Mon. Not. R. Astron. Soc. **000**, 1–14 () Printed 20 October 2015 (MN LATEX style file v2.2)

Erasing the Milky Way: new cleaning technique applied to GBT intensity mapping data

L. Wolz[1,2⋆], C. Blake[3], F. B. Abdalla[4], C.M. Anderson[5], T.-C. Chang[6], Y.-C. Li[7], K.W. Masui[8,9], E. Switzer[10], U.-L. Pen[11], T.C. Voytek[12], J. Yadav[13]

[1] *School of Physics, University of Melbourne, Parkville, VIC 3010, Australia*
[2] *ARC Centre of Excellence for All-Sky Astrophysics (CAASTRO)*
[3] *Centre for Astrophysics & Supercomputing, Swinburne University of Technology, P.O. Box 218, Hawthorn, VIC 3122, Australia*
[4] *Department of Physics and Astronomy, University College London, London WC1E6BT, UK*
[5] *Department of Physics, University of Wisconsin - Madison, Madison, WI, USA*
[6] *Academia Sinica Institute of Astronomy and Astrophysics, P.O. Box 23-141,Taipei, 10617 Taiwan*
[7] *National Astronomical Observatories, Chinese Academy of Sciences, 20A Datun Road, Chaoyang District, Beijing 100012, China*
[8] *Department of Physics and Astronomy, University of British Columbia, 6224 Agricultural Rd. Vancouver, V6T 1Z1, Canada*
[9] *Canadian Institute for Advanced Research, CIFAR Program in Cosmology and Gravity, Toronto, ON, M5G 1Z8*
[10] *NASA Goddard Space Flight Center, Greenbelt, MD 20771, USA*
[11] *Canadian Institute for Theoretical Astrophysics, 60 St. George Street,Toronto, ON M5S 3H8, Canada*
[12] *Astrophysics and Cosmology Research Unit, School of Chemistry and Physics, University of KwaZulu-Natal, Durban, 4041, South Africa*
[13] *Sri Aurobindo College, University of Delhi, Malviya Nagar, New Delhi 110017, India*

arXiv:1510.05453v1 [astro-ph.CO] 19 Oct 2015

ABSTRACT

We present the first application of a new foreground removal pipeline to the current leading HI intensity mapping dataset, obtained by the Green Bank Telescope (GBT). We study the 15hr and 1hr field data of the GBT observations previously presented in Masui et al. (2013) and Switzer et al. (2013) covering about 41 square degrees at $0.6 < z < 1.0$ which overlaps with the WiggleZ galaxy survey employed for the cross-correlation with the maps. In the presented pipeline, we subtract the Galactic foreground continuum and the point source contaminations using an independent component analysis technique (FASTICA) and develop a description for a Fourier-based optimal weighting estimator to compute the temperature power spectrum of the intensity maps and cross-correlation with the galaxy survey data. We show that FASTICA is a reliable tool to subtract diffuse and point-source emission by using the non-Gaussian nature of their probability functions. The power spectra of the intensity maps and the cross-correlation with WiggleZ is typically an order of magnitude higher than the previous findings by the GBT team. FASTICA is a very conservative subtraction technique and is not able to remove anisotropic noise contaminations caused by instrumental systematics unlike the singular value decomposition method which does not discriminate components according to their statistical properties. We confirm that foreground subtraction with FASTICA is robust against 21cm signal loss as seen by the converged amplitude of the cross-correlation of the intensity maps with the WiggleZ data.

Key words: cosmology – statistical methods – radio astronomy – large-scale structure.

1 INTRODUCTION

Cosmological observations aim to map the largest possible volume of the Universe in order to develop a better understanding of the formation and evolution of large-scale structure. The clustering of galaxies traces the dark matter distribution, and thus the laws of gravity, in addition to the time-dependent expansion of the Universe driven by Dark Energy, both the major ingredients of the standard model of cosmology. Historically, optical galaxy surveys, such as Sloan Digital Sky Survey (Tegmark et al. 2004) or WiggleZ (Drinkwater et al. 2010), are used to observe the skies and catalogue the galaxies in angular and redshift position. While achieving major scientific discoveries such as the detection of the Baryon Acoustic Oscillations (BAO) (Eisenstein et al. 2005; Percival et al. 2007; Percival et al. 2010),

⋆ E-mail:lwolz@unimelb.edu.au

© RAS

this approach is affected by, for instance, selection effects and redshift inaccuracies for photometric surveys or low survey efficiency for spectral observations.

Galaxy surveys in the radio wavelength, as opposed to the optical spectrum, have limited feasibility due to their spatial resolution limitations. However, with recent advances in radio interferometry, both instrumental and algorithmic, forthcoming radio surveys have high prospects. In addition to the traditional galaxy surveys, a new observational method called intensity mapping has been formulated with the main objective to measure the large-scale structure, see e.g. Battye et al. (2004); Vujanovic et al. (2009); Peterson & Suarez (2012); Bull et al. (2014) . This technique exploits the low angular resolution of radio telescopes by efficiently mapping the structure via their integrated spectral line emission with a beam small enough to resolve the BAO scale. The neutral hydrogen line (HI) at 21cm is assumed to be an excellent tracer for the galaxy distribution and, in addition, not prone to line confusion (Gong et al. 2011). Intensity mapping has also been envisaged using different spectral lines such as the rotational CO lines (Lidz et al. 2011) or Lyman-alpha line (Pullen et al. 2013).

In comparison to the galaxy surveys, intensity mapping has the advantage of measuring the entire HI flux in the observed frequency channel. This implies that there are no observational selection effects, which allows access to a wide redshift range, and the integrated luminosity function is probed rather than the most luminous objects. The downside of intensity mapping are the high demands on the instrumental stability for a robust continuous mapping and the high Galactic foregrounds which dominate the targeted frequency ranges.

The challenge of Galactic foreground subtraction has been extensively addressed in the framework of Cosmic Microwave Background (CMB) observations, see Planck Collaboration X, (2015) and Planck Collaboration XXV, (2015) for the latest results. In intensity mapping, the foregrounds are less spatially constrained by observations than in the microwave sky, however, the data contains more line-of-sight information as it extends over a considerably wider frequency interval. Most foreground separation methods utilise the power-law dependence of the foregrounds in the frequency direction where the techniques can be divided in parametric (Ansari et al. 2008; Shaw et al. 2014,?) and blind methods (Wolz et al. 2014; Switzer et al. 2015). In this work, the foreground subtraction is performed by an independent component analysis (FASTICA by Hyvärinen 1999) motivated by previous, successful applications to CMB data, e.g. in Maino et al. (2002), a epoch of reionization study in Chapman et al. (2012) and intensity mapping simulations in Wolz et al. (2014).

After promising theoretical predictions of intensity mapping surveys (Wyithe et al. 2007; Chang et al. 2008), the Green Bank Telescope (GBT) team has pioneered in the realisation of an experiment and data analysis as shown in Chang et al. (2010), Masui et al. (2013) (MA13 hereafter) and Switzer et al. (2013) (SW13 hereafter). The foreground removal as presented in SW13 is based on a singular value decomposition (SVD) where the highest eigenvalues assumed to contain the foregrounds and are subtracted from the data. MA13 shows the detection of the intensity mapping signal through cross-correlation with the WiggleZ galaxy survey which is used in combination with the auto power spectrum to constrain the amplitude of the correlation to $\Omega_{\rm HI} b_{\rm HI} = [0.62 \pm 0.23] \times 10^{-3}$at 68% confidence level in SW13 where $\Omega_{\rm HI}$ is the neutral hydrogen energy density and $b_{\rm HI}$ is the HI bias parameter.

In this work, we apply our foreground removal and power spectrum estimator pipeline to the GBT datasets and demonstrate how FASTICA can reliably subtract foregrounds, in addition to providing insight into the signal properties.

The following work is structured as follows: Sec.2 briefly outlines the data specifications of the GBT observations and the WiggleZ galaxy survey. Sec.3 describes the Fourier-based power spectrum estimator for the auto- and cross-correlations. The following section 4 presents a detailed analysis of the component separation and the data properties as seen by this analysis. In Sec.5, the intensity mapping power spectrum and the cross-correlation with WiggleZ are given in comparison with the GBT results. We conclude in Sec.6.

2 OBSERVATIONS

2.1 Green Bank Telescope Intensity Maps

The detailed description of the observing strategy of the analyzed intensity maps can be found in MA13 .

In this work, we analyze the intensity maps consisting of a $4.5\,\mathrm{deg} \times 2.4\,\mathrm{deg}$ "15hr deep field" centered at 14h31m28.5s RA and $2\,\mathrm{deg}\,0'$ DEC which was observed with 105h integration time and a $7.0\,\mathrm{deg} \times 4.3\,\mathrm{deg}$ "1hr wide field" centered at 0h52m0s RA and $2\,\mathrm{deg}\,9'$ DEC with 85h integration time. Each of the fields was observed in 4 sub-datasets $\{\mathrm{A}, \mathrm{B}, \mathrm{C}, \mathrm{D}\}$ which have similar integration time and sky coverage. The sub-set maps were taken at different times such that the thermal noise of the instrument is independent in each map.

The data was taken between 700MHz and 900 MHz, i.e. $0.58 < z < 1$, divided into 4096 channels across the bandwidth. The data is rebinned into bands with 0.78MHz width which is equivalent to $3.8h^{-1}$Mpc comoving width along the line of sight at the band center. The total calibration uncertainty is 9%. The map-making conventions of the GBT team follow the CMB description given in Tegmark (1997). The pixels of the maps are square with length of 0.0627 deg and dimensions 78×43 for the 15hr-field and 161×83 for the 1hr-field. The beam has a co-moving width of approximately $9.6h^{-1}$Mpc at the band center. The effective beam shape of the GBT is influenced by polarization leakage which is mitigated by convolving the data to an effective beam with $\theta_{\rm FWHM} = 0.44\,\mathrm{deg}$.

2.2 WiggleZ galaxy survey

The WiggleZ Survey (Drinkwater et al. 2010) is a large-scale galaxy redshift survey of bright emission-line galaxies over the redshift range $z < 1$, with median redshift $z \approx 0.6$ and galaxy bias factor $b \sim 1$. The survey was carried out at the Anglo-Australian Telescope between August 2006 and January 2011. In total $\sim$ 200,000 redshifts were obtained, covering $\sim$ 1000 deg^2 of equatorial sky divided into seven well-separated regions. The two GBT fields analyzed in this study have nearly complete angular and redshift overlap

with two of these WiggleZ regions, and the two datasets are therefore very well-suited for cross-correlation analysis. Following the cut to the redshift range $0.58 < z < 1$, a total of 6731 WiggleZ galaxies are used in this analysis. The WiggleZ selection function within each region, which is used to produce the optimal weighting for our power spectrum analysis, was determined using the methods described by Blake et al. (2010) by averaging over a very large number of random realizations.

3 POWER SPECTRUM MEASUREMENT

3.1 Optimal weighted power spectrum estimator

The present GBT intensity mapping data covers a very small fraction of the sky, and allows us to apply a "flat-sky approximation" where we map the angular and redshift pixels onto a cuboid in comoving space using a fiducial cosmology. For the following analysis, the power spectrum is approximated in flat comoving coordinates where we follow the description and the notational conventions in Blake et al. (2010) and Blake et al. (2013). We recast the description in terms of temperature power spectra of intensity maps with a weighting scheme dictated by the noise properties of the observations. We formulate the equations as discrete functions in pixel space, however, the reader should keep in mind that every pixel is associated with a three-dimensional vector $\vec{x}$ or $\vec{k}$ respectively.

We consider the intensity maps measured as a discrete function $\delta(\vec{x}_i)$. Each map pixel is given as an overtemperature $\delta(\vec{x}_i) = T(\vec{x}_i) - \bar{T}$ in units of mK where $\bar{T}$ is mean temperature of each frequency slice. The dimensions of the data are (N_x, M_y, K_z), where N_x and M_y are fixed dimensions given by the map-making process. K_z is the total number of maps in frequency employed to estimate the power spectrum and has to be small enough such that the flat sky approximation holds. The total number of pixels is $N_{pix} = N_x \cdot M_y \cdot K_z$. The size of each pixel is determined by the comoving length L_x and L_y. The radial size L_z is determined by the bandwidth of the observations neglecting the slow variation of the comoving width of each frequency slice with redshift. The physical comoving volume of the grid $V_{\rm cell} = \frac{L_x \cdot L_y \cdot L_z}{N_x M_y K_z}$ is calculated using a fiducial cosmological model with parameters $\vec{\theta} = (h = 0.73, \Omega_{\rm m} = 0.25, \Omega_{\rm b} = 0.045, n_{\rm s} = 1.0, \sigma_8 = 0.9)$.

The Fourier-transformed temperature field is a function of the wavevector $\vec{k}_l$. The resolution of the measurements in Fourier-space is given by $\Delta k_x = 2\pi/L_x$, $\Delta k_y = 2\pi/L_y$ and $\Delta k_z = 2\pi/L_z$. The upper bound on $\vec{k}_l$, which refers to the smallest scale in real space which can be measured in our grid, is determined by the Nyquist frequency in each direction $k_{\rm Nyq,x} = \pi \cdot N_x/L_x$, $k_{\rm Nyq,y} = \pi \cdot M_y/L_y$ and $k_{\rm Nyq,z} = \pi \cdot K_z/L_z$ above which information is not accessible. The Fourier amplitudes for each mode are calculated via

$$\tilde{\delta}(\vec{k}_l) = \sum_{j=1}^{N_{pix}} \delta(\vec{x}_j) w(\vec{x}_j) \exp\left(i\vec{k}_l \cdot \vec{x}_j\right). \quad (1)$$

The temperature of each pixel is multiplied by an weighting function $w(\vec{x}_j)$ which is chosen to be normalised such that $\sum_{i=1}^{N_{pix}} w(\vec{x}_i) = 1$ in the estimators given below.

In the case of noise-dominated intensity mapping data, the weighting function is directly related to the noise in each pixel. We consider a simple inverse-variance weighting using this noise map.

Under the assumption that the noise is uncorrelated the estimate of the power spectrum for each Fourier amplitude in volume units is

$$P_{\rm est}(\vec{k}_l) = \frac{V_{\rm cell} |\tilde{\delta}(\vec{k}_l)|^2}{\sum_{j=1}^{N_{pix}} w^2(\vec{x}_j)} \quad (2)$$

where we neglect the correction terms for the noise contribution which would in general be subtracted. In our analysis, we estimate the cross-power spectra of every pair of different sub-dataset maps to suppress this thermal noise correction term. We bin amplitudes of Fourier modes $\vec{k}$ according to the value of $k = |\vec{k}|$ in bins. The cross-power spectrum for two intensity mapping datasets A and B is

$$P^{AB}_{\rm est}(\vec{k}_l) = \frac{V_{\rm cell} {\rm Re}\{\tilde{\delta}^A(\vec{k}_l) \cdot \tilde{\delta}^B(\vec{k}_l)^*\}}{\sum_{j=1}^{N_{pix}} w^A(\vec{x}_j) \cdot w^B(\vec{x}_j)} \quad (3)$$

The above equation for the cross-correlation between two intensity mapping datasets can be recast for the cross-correlation with galaxy survey data $P^{\rm X}_{\rm est}(\vec{k}_l)$ where the over density is defined as number of galaxies per voxel N_i divided by the mean galaxy density of the cube $\bar{N}$, $\delta_{\rm g}(\vec{x}_i) = N_i/\bar{N}$. The optimal weighting function $w_{\rm g}(\vec{x}_i) = 1/(1 + W(\vec{x}_i) \times \bar{N} P_0)$ is computed via the selection function $W(\vec{x}_i)$ given by (Blake et al. 2010) with $P_0 = 10^3 h^{-3}{\rm Mpc}^3$.

In addition, we need to take into account the telescope beam via dividing the $\hat{P}(\vec{k}_i)$ by the discretized, Fourier transformed beam $\tilde{B}(\vec{k}_i)$ where $B(\vec{x}_j)$ is set up as a spatial, 2-dimensional Gaussian beam discretized on the grid such that it only acts on perpendicular modes of the power spectrum.

The thermal noise contributes to errors in the cross-power spectrum measurements. For noise dominated data, the cosmic variance contribution can be neglected. Under the assumption that the noise has similar properties in each datasets, we can estimate the variance on the intensity mapping cross-correlation as (compare e.g. White et al. 2009)

$$\sigma(P^{AB}_{\rm est}(k_i)) = P_{\rm noise}(k_i)/\sqrt{2 \cdot N(k_i)} \quad (4)$$

where the noise power spectrum $P_{\rm noise}$ is scaled with $\sqrt{2}$ since two independent maps are correlated and $N(k_l)$ is the number of independent measured modes per k_l bin. There are various ways to estimate $P_{\rm noise}$ which will be explained in Sec. 5.

The covariance on the cross-correlation can be estimated using the estimated galaxy power spectrum $P^{\rm g}_{\rm est}$ and the intensity mapping power spectrum $P^{AB}_{\rm est}$

$$\sigma(P^{\rm X}_{\rm est}(k_i)) = \sqrt{\frac{(P^{\rm X}_{\rm est}(k_i))^2}{2 \cdot N(k_i)} + P^{\rm g}_{\rm est}(k_i) P^{AB}_{\rm est}(k_i)} \quad (5)$$

In this work, we will present the power spectra in a dimensionless form

$$\Delta^2(k_i) = \frac{k_i^3}{2\pi^2} P(k_i). \quad (6)$$

3.2 Theoretical prediction

We compare the measured power spectrum of the intensity maps to a theoretical prediction $P_{\rm th}(k)$. We use the linear 3d

CAMB (Lewis et al. 2000) power spectrum and multiply it with the growth function for $z = 0.8$. The weighting scheme of the temperature power spectrum alters the shape of the power spectrum. In order to account for this effect, we convolve the theoretical prediction with the weighting function via

$$\hat{P}_{\rm th}(\vec{k}_j) = \frac{\sum_i P_{\rm th}(\vec{k}_i')\mathrm{Re}\{\tilde{w}_A(\vec{k}_j - \vec{k}_i)\tilde{w}_B(\vec{k}_j - \vec{k}_i)^*\}}{\sum_{j=1}^{N_{pix}} w^A(\vec{x}_j)w^B(\vec{x}_j)}. \quad (7)$$

For this computation, we grid the smooth 1-dimensional $P_{\rm th}(k)$ onto the same grid as the intensity maps, hence discretize the modes as $P_{\rm th}(\vec{k}_j)$.

The estimated power spectrum of the intensity maps relates to the theory as $P_{\rm est} = b_{\rm HI}^2 \bar{T}_{\rm HI}^2 P_{\rm th}$ where we use Equ. 1 in MA13 as a model for the mean HI temperature which predicts $\bar{T}_{\rm HI} = 0.29{\rm mK} \times \Omega_{\rm HI}/10^{-3}$ for the fiducial cosmology at band centre such that $P_{\rm est} = b_{\rm HI}^2 \Omega_{\rm HI}^2 P_{\rm th}$. The factor $b_{\rm HI}\Omega_{\rm HI}$ is chosen according to the cross-correlation measurements with the WiggleZ data in MA13 as 0.43×10^{-3}. We note that this is a lower limit because of the unknown cross-correlation coefficient r between HI and galaxy overdensity. The cross-correlation $P_{\rm est}^{\rm X} = b_{\rm HI} b_{\rm opt} \Omega_{\rm HI} r P_{\rm th}$ depends additionally on the optical bias which is assumed as $b_{\rm opt}^2 = 1.48$ according to measurements in Blake et al. (2010).

4 FOREGROUND REMOVAL AND SYSTEMATICS ANALYSIS

4.1 fastica application

We apply the FASTICA to the intensity mapping data cube in order to remove the foregrounds, where we solve the linear problem

$$\boldsymbol{x} = \mathbf{A}\boldsymbol{s} + \epsilon = \sum_{i=1}^{N_{\rm IC}} \boldsymbol{a_i} s_i + \epsilon, \quad (8)$$

where $\boldsymbol{x}$ is the input data, $\mathbf{A}$ the mixing matrix and $\boldsymbol{s}$ represent the independent component amplitudes (ICs). The ICs can be seen as maps with the same spatial dimension as the intensity maps. The amplitude of each IC i per frequency is given by the mixing modes $\boldsymbol{a_i}$. The FASTICA identifies components with strong spectral correlation and incorporates them into the ICs by using the Central Limit theorem such that it maximises the Non-Gaussianity of the probability density function of each IC. This implies by definition that FASTICA neglects Gaussian distributions such that the component separation via $\mathbf{A}\boldsymbol{s}$ only incorporates the foregrounds. The residual of the analysis ϵ contains foreground-subtracted data cube which ideally contains 21cm signal and noise but in principle can contain residual foregrounds as well. We refer the reader to Wolz et al. (2014) for a more detailed description.

The number of ICs (N_{IC}) used in the component separation is a free parameter and can not be determined by the FASTICA itself. In this section, we carefully examine the data after the foreground subtraction for cases with different numbers of ICs. We present a range of different tests of systematics for many cases and discuss how to correctly choose the number of ICs such that the results do not sensitively depend on this choice.

4.2 Foreground point source removal

The data maps exhibit prominent spatial features caused by point source contamination of extra-Galactic sources which are present throughout all frequencies. The FASTICA models the spatial structure of the foregrounds as well as their frequency dependence. In Fig. 1, we present the maps of the ICs for the sub-dataset A of the 15hr-field where an analysis with 2, 6 and 10 ICs is shown. We show the IC maps for a full spatial analysis in the first column. In these maps, the FASTICA mainly models dominant features at the edges of the data maps which are partly caused by very high instrumental noise due to the poor observational coverage of the edges. The IC maps do not optimally model the point source structure and diffuse foregrounds because of the high noise contamination. By masking out those regions as seen in the second column of Fig. 1, the ICs clearly contain the spatial structure of the point sources of Galactic foregrounds. We observe similar behaviour of the ICs for the remaining datasets and the 1hr-field analysis. For our results, we use the masked data cubes as a default.

Furthermore, we examine the residual maps of the analysis for point source contamination in all frequencies. The accuracy of the removal can be checked by adding up the residual maps over all frequencies. The noise and the cosmological signal are close to Gaussian distributed with low correlations across frequency. Therefore those components are expected to show no spatial structure when averaging over many frequencies. In Fig. 2, the sum of all residual maps of the sub-dataset A of the 15hr-field is shown for different number of ICs. The analysis of the full maps is shown in the first columns and the masked maps in the second column. The full maps show again how the high noise at the edges is not fully modelled by FASTICA. For the masked analysis with two ICs as seen in panel (b), the added maps contain point source residuals. Those residuals fade out with increasing number of ICs until they are clearly removed for 10 ICs in panel (f). These tests evidently show how the FASTICA is able to model and subtract the strong point sources from the intensity maps for $N_{\rm IC} \geqslant 6$.

The 1hr-field observations contain less strong point sources, however suffer from very inhomogeneous noise properties due to shorter integration times. Although FASTICA can not fully model the systematic effects with close to Gaussian distributions, the individual sub-datasets exhibit different spatial noise imprints such that their effect on the cross-correlation between the maps should be diminished.

4.3 Calibration or instrumental resonance

Some frequency channels of the GBT telescope are sensitive to telescope resonance or RFI. In addition, the calibration of the telescope is a source of error in the amplitude of the measurements. In Fig. 3, the mixing modes $\boldsymbol{a_i}$ which give the mixing amplitude per frequency channel, are plotted for an analysis of one dataset of the 15hr-field with 2, 6 and 10 ICs as a function of frequency bin. Note that frequency bin 0 refers to $f = 900$MHz, i.e. $z = 0.58$. In a perfect foreground subtraction scenario, each line should represent the flat spectral index of a foreground component. Through instrumental effects like calibration errors, varying thermal noise, frequency-dependent polarization errors

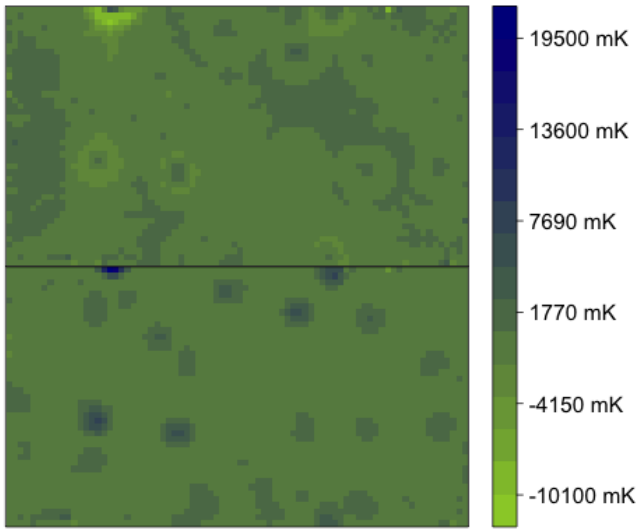

(a) 2 ICs

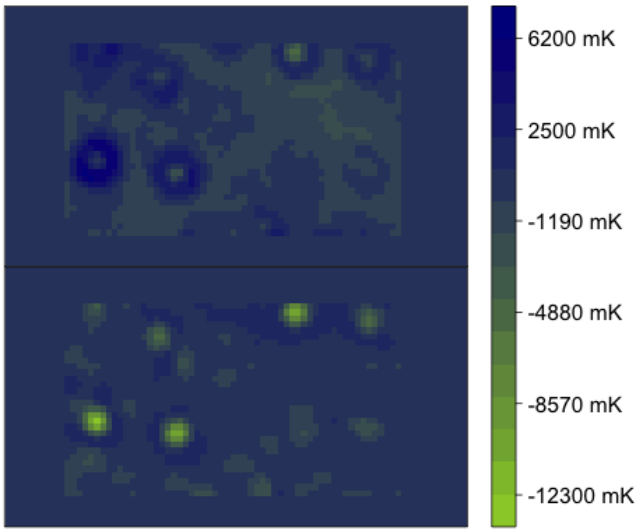

(b) 2 ICs; masked

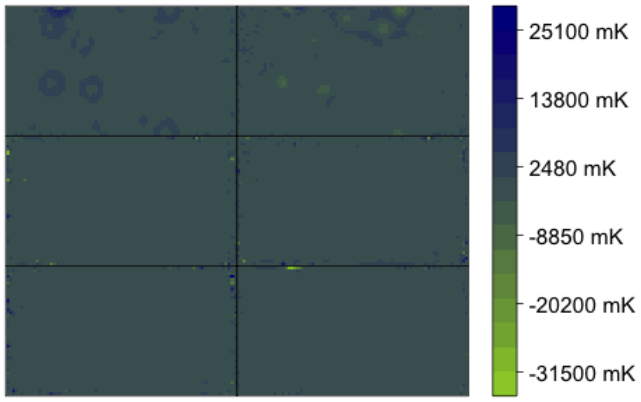

(c) 6 ICs

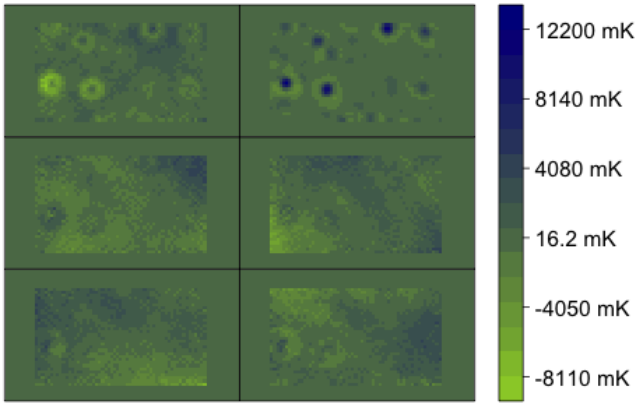

(d) 6 ICs; masked

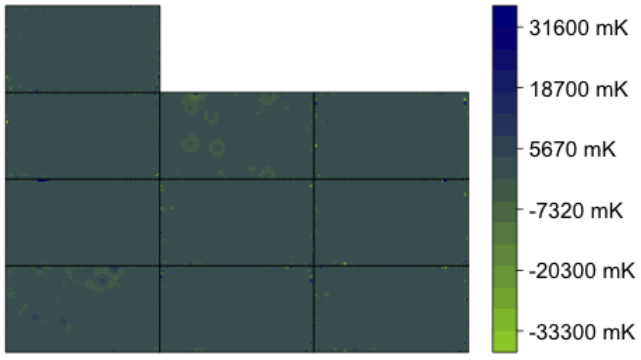

(e) 10 ICs

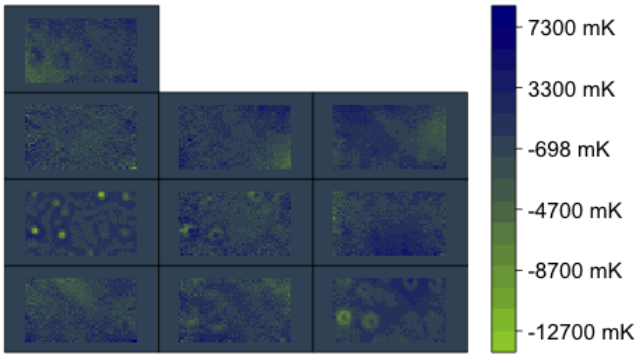

(f) 10 ICs; masked

Figure 1. The maps of the independent components for an analysis on the full maps in the first column and for a masked analysis with the noise-dominated edges disregarded. The ICs for an analysis of the dataset A of the 15hr-field are presented as an example.

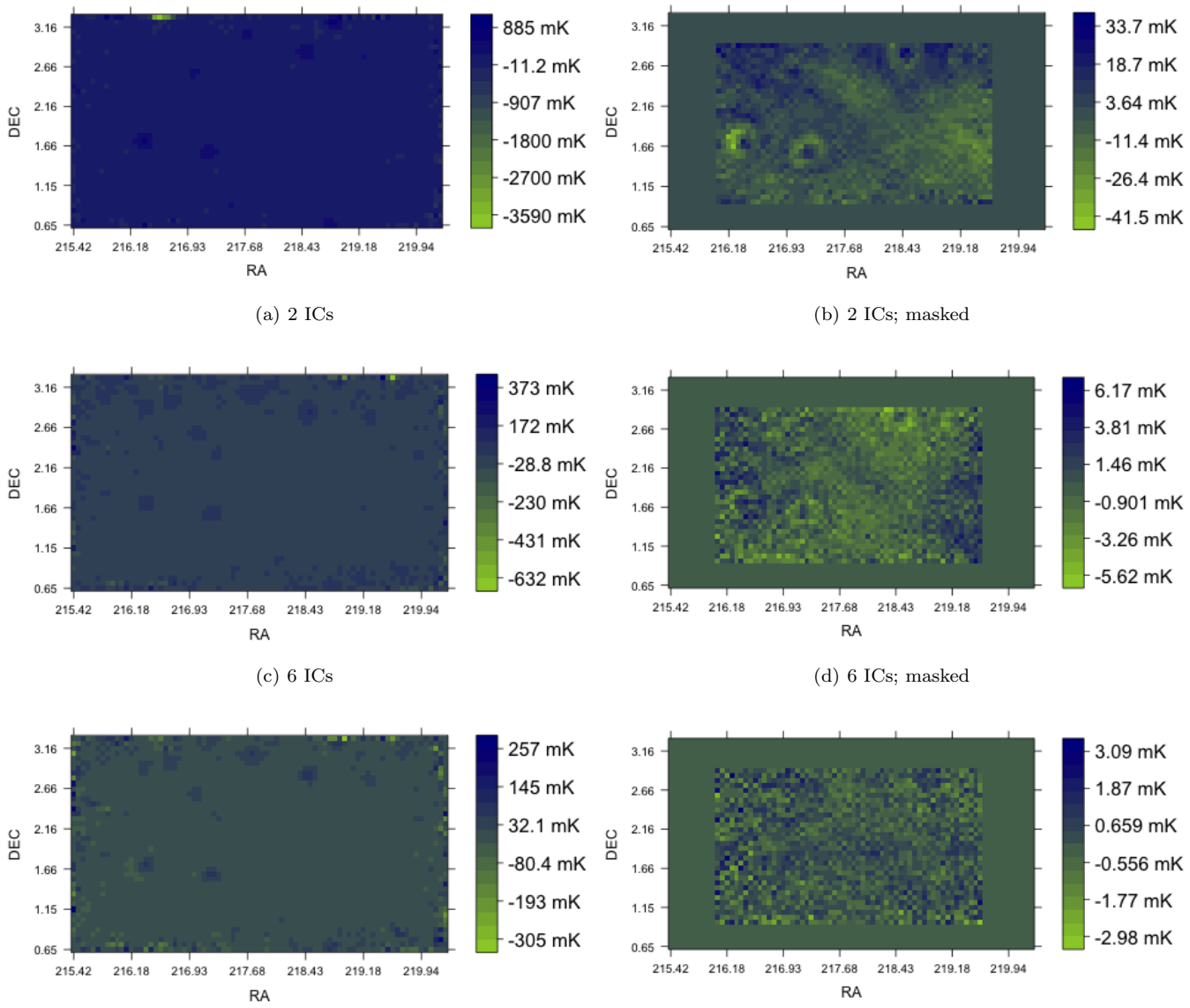

(a) 2 ICs

(b) 2 ICs; masked

(c) 6 ICs

(d) 6 ICs; masked

(e) 10 ICs

(f) 10 ICs; masked

Figure 2. The temperature residual maps of the sub-dataset A of the 15hr-field are summed up over all frequency channels. The residual maps after the foreground removal with FASTICA should only contain noise and 21cm signal. The maps in the first column show the sums for a full analysis and the second column shows masked results.

and telescope resonances the flat spectra are disturbed and corrupted data can be identified. Around the frequencies 798MHz and 817MHz, two known telescope resonances corrupt the measurements which have been flagged during the map-making. These maps can be seen as the very high spikes in panels (a), (b) and (c) where we performed the FASTICA on the full data set. We removed the contaminated frequency maps and the first frequency bins which show anomalies probably due to calibration uncertainties. The results of the mixing modes are shown in panels (d), (e) and (f). One mixing mode spectrum for 2 ICs exhibit two features for high frequency bins which point to an irregularity in the data due to instrumental effects. In panel (d) and (e) for 6 and 10 ICs, we observe that some modes show very high fluctuations around a flat spectrum. These large amplitude oscillations around zero are due to the fact that the FASTICA has picked up dominant noise features and tries to model them as ICs. We solve this issue by masking the maps cutting the edges which contain very high noise. The results are shown in panels (g), (h) and (i). The mixing modes are now relatively flat and featureless. We are therefore confident that the FASTICA predominately picks up frequency-dependent foreground components and the masked analysis with pixel dimensions 58×33 is set as the fiducial for the remainder of this work.

The analysis of the 1hr field exhibits similar improvements when masking out the edges. The mixing modes of the 1hr-field are slightly more fluctuating since FASTICA attempts to model the strong noise features present in these

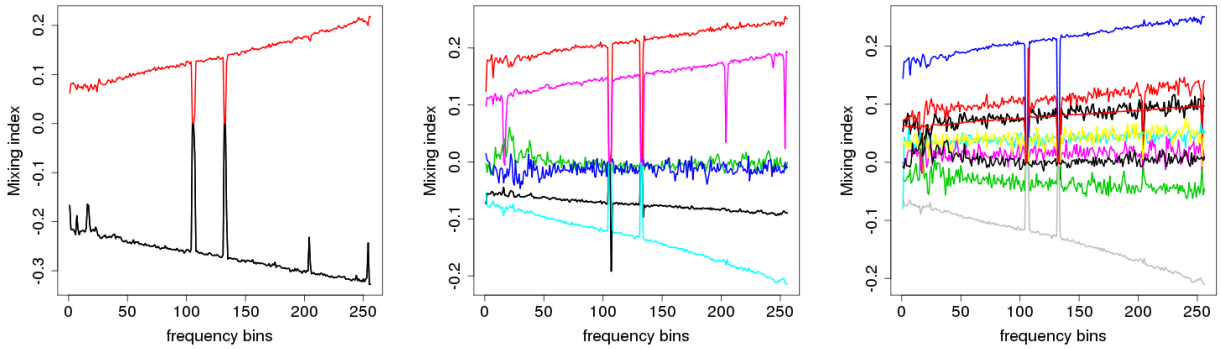

(a) res.; 2 ICs (b) res.; 6 ICs (c) res.; 10 ICs

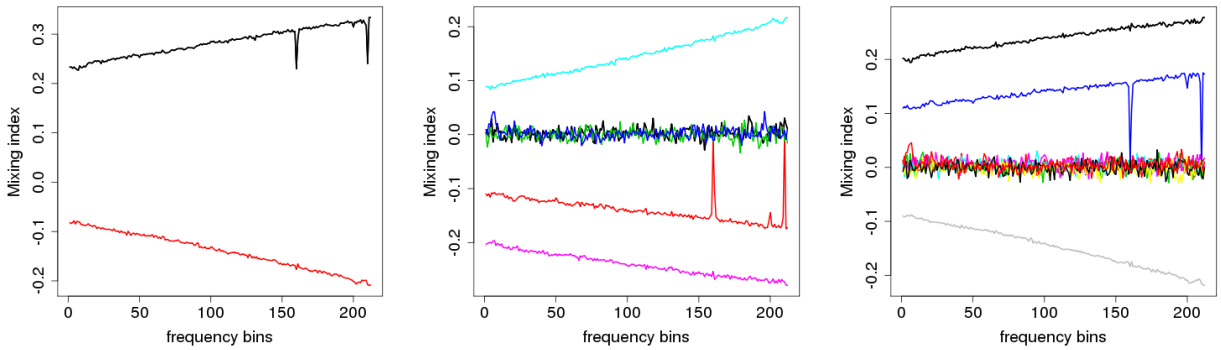

(d) no res.; 2 ICs (e) no res.; 6 ICs (f) no res.; 10 ICs

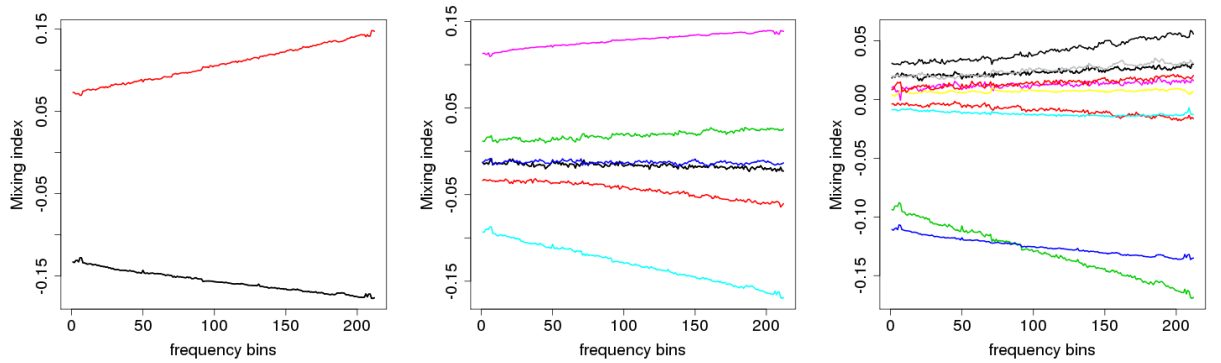

(g) no res.; masked; 2 ICs (h) no res.; masked; 6 ICs (i) no res.; masked; 10 ICs

Figure 3. The columns of the mixing matrix **A** plotted along the line-of-sight as a function of frequency bins for an analysis of subdataset A of the 15hr-field. The first column shows an analysis with 2 ICs, the second one for 6 ICs and the third one for 10 ICs. The first row considers the full data set. For the analysis shown in the second row, the instrument resonance contaminated frequency maps and the first frequency maps are removed. In the third row, additionally, the noise dominated edges of each map are masked out. A smoothly-varying dependence on frequency is then produced which is aimed for in an optimal foreground subtraction.

observations. The default mask of the 1hr-field results in 121×53 pixels.

4.4 Noise properties

In Fig. 4, we show the standard deviation of the residual maps along the line of sight. For noise dominated data, we expect the standard deviation to be much higher than the amplitude of the sum of all pixels as can be seen when comparing the deviation with Fig. 2. The structure of the standard deviation maps additionally shows how the noise varies with spatial position. For the dataset A of the 15hr-field in Fig. 4, the maps show very stable amplitudes and spatial structure when increasing N_{IC} from 2 to 6 and 10. This

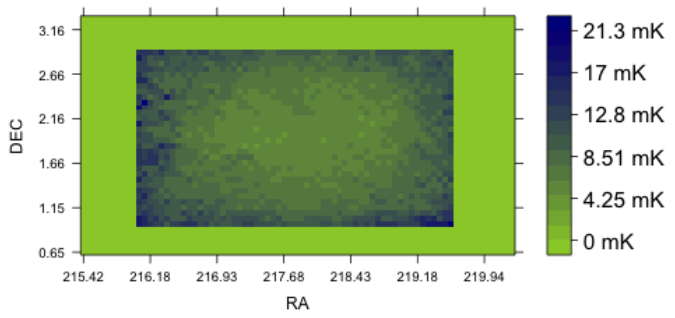

(a) 2 ICs

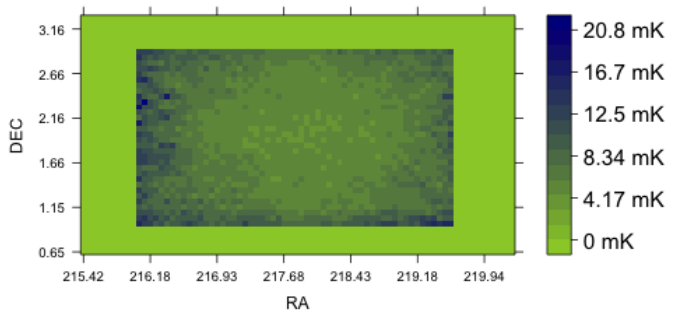

(b) 6 ICs

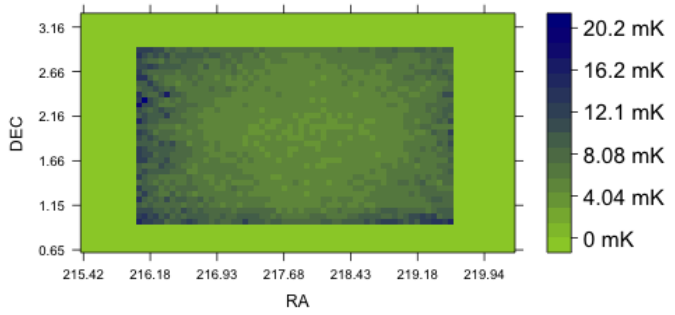

(c) 10 ICs

Figure 4. The standard deviation of each line-of-sight pixel of the temperature residual maps of the FASTICA in units of K of the sub-dataset A of the 15hr-field are shown as a probe of the noise properties. The standard deviations can be seen unaffected by the number of ICs chosen.

can be interpreted as very low noise leakage into the reconstructed Galactic foregrounds and confirms the Gaussian nature of the instrumental noise.

The noise levels of the residuals of the 1hr-field maps are less stable with increasing number of ICs than the 15hr-field. The noise properties are dominated by single features with irregular distribution over the map due to the differing observational depth of the pixels. FASTICA can incorporate some of the strong features as ICs and remove parts of the noise systematics. We note that the noise structure of each sub-dataset differs, which prevents contamination of the cross-correlation.

We access more information about the structure of the data by measuring the spatial 2d power spectrum auto- or cross-correlation of individual frequency maps employing the the same formalism as in Sec. 3, using two dimensions of the data. Fourier transformed temperature maps are calculated as $\tilde{T}_A(\vec{k}_l) = \sum_{j=1}^{N_{pix}} T_A(\vec{x}_j) \exp(i\vec{k}_l \cdot \vec{x}_j)$. The spatial power spectrum is defined as $P_{2d}(\vec{k}_l) = \mathrm{Re}\{\tilde{T}_A(\vec{k}_l)\tilde{T}_B(\vec{k}_l)^*\}$. The spatial noise power spectrum of one frequency map can be estimated via two measures:

- A jack-knife test: the difference of two sub-datasets should only contain thermal noise since the astrophysical signal remains the same with time. We obtain an estimate for the noise power spectrum of one map via calculating the power spectrum of the difference map and dividing it by two. The difference maps also exhibit systematic effects of the sub-datasets.
- Auto-correlation: the power spectrum of each sub-dataset after the foreground removal should be a proxy for the noise if it dominates the HI signal.

In Fig. 5, we show a few examples of the 2d power spectra of the difference-maps and the auto-correlations of the 15hr-field where we averaged over all possible combinations of sub-datasets. It can be seen that the difference-map correlations have more power than the auto-correlations. This can be explained by considering the spatial structure of the difference maps in Fig. 6. The maps show a clear structure at the position of the point sources which indicates instrumental effects, like calibration errors, pointing offsets and thermal noise which correlates with the amplitude of signal. The amplitude of the contaminated pixels does not show a frequency dependence but a flat spectrum along the line-of-sight. The FASTICA models the point sources in each sub-dataset independently and can remove those systematic effects. Hence, in Fig. 5, we show a maximum noise variance by the difference map which partly includes systematic effects. The analysis of the 1hr-field shows similar behaviour of the power spectrum of the difference maps compared to the auto-correlation of the residual maps.

4.5 Residual-foreground correlation

For the evaluation of the foreground removal, we consider the spatial 2d power spectrum of the cross-correlation of different frequency maps. In the following plots, we show two kinds of correlations:

- The cross-correlation of the residual maps from different sub-datasets. This cross-correlation should be driven by the cosmological signal since the noise is uncorrelated between sub-datasets, however, could give evidence to residual foreground contaminations.
- The cross-correlation of the residuals and the reconstructed foreground maps: the residual-reconstruction cross-correlation is a measure of the foreground subtraction errors. In addition, if the foregrounds are insufficiently modeled, the residuals will be contaminated. The FASTICA possibly partly models instrumental noise or cosmological signal within the ICs.

In Fig. 7, we show the spatial 2d power spectra of the cross-correlation of frequency maps as a function of scale for an unmasked FASTICA in the first column and a masked in the second column. The cross-correlations are measured for maps

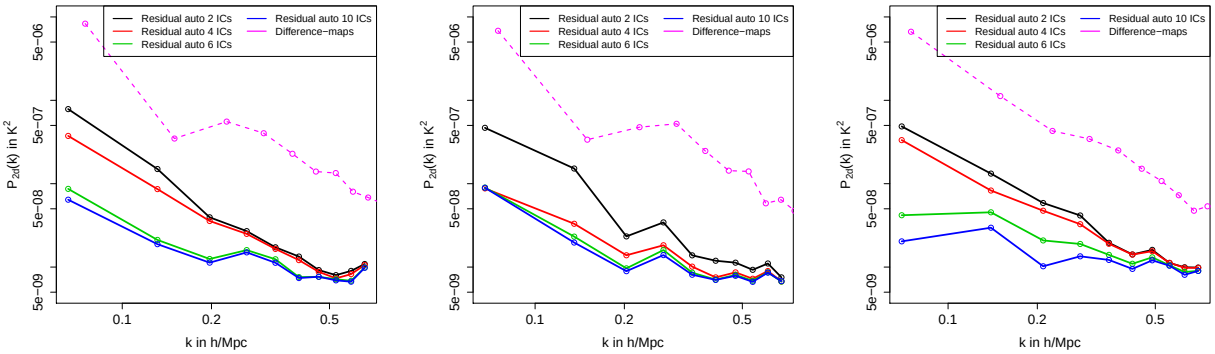

(a) $\nu = 838$MHz (b) $\nu = 806$MHz (c) $\nu = 775$MHz

Figure 5. Spatial, 2d auto correlations of the residual maps of the 15hr-field for different ICs (solid lines) in comparison to the difference-map power spectrum of the original maps (dashed). Each power spectrum is averaged of all possible combinations of sub-datasets. Each of these power spectra can be seen as a noise approximation of the maps before and after the foreground removal.

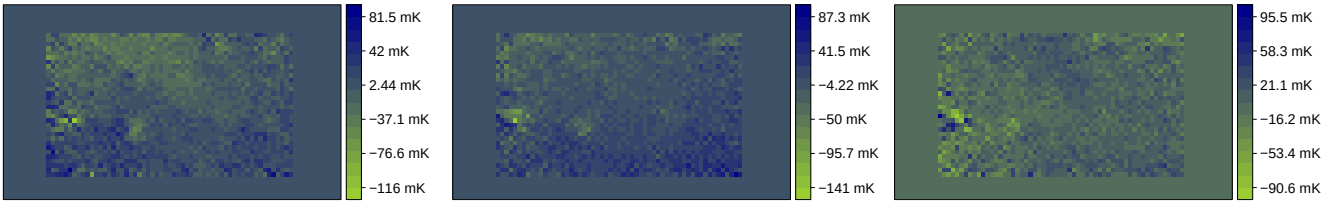

(a) Sub-dataset (A - B) (b) Sub-dataset (A - C) (c) Sub-dataset (B - C)

Figure 6. The difference maps of the 15hr-field observations shown for frequency $\nu = 869$MHz. The difference maps exhibit clearly spatial structure due to systematic errors in the sub-datasets.

where we stacked 20 frequency bins. As shown in the previous paragraphs, the maps are dominated by thermal noise. When adding N noise realisations of different frequencies, the noise decreases as $1/\sqrt{N}$.

The amplitudes of the cross-correlations are proportional to the multiplication of mean temperatures of the two input maps. In order to compare the cross-correlation of foreground and residuals to the correlation of residual maps, we need to normalize the amplitude. The reconstructed foreground maps and the residual maps scale with different mean temperatures which are unknown. Therefore, the cross-correlations are normalised by the standard deviations of the respective maps.

In the first column, the figures show the results of the flawed FASTICA decomposition which insufficiently removes the point sources of the foregrounds, as seen in the stacked maps in Fig. 2. The solid lines show a very similar behaviour for different number of ICs and frequencies, indicating a correlation between foregrounds and residuals. In the second column, the masked results which are clean of point source contamination are shown. The cross-correlation of foreground and residuals are relatively random distributed and are an indication that the data is dominated by statistical noise not systematic foregrounds. The dashed lines in all figures are the residual correlation between all combinations of sub-datasets. It can be seen that they converge for increasing number of ICs which confirms the results of the successful foreground removal of previous tests and show that our results do not sensitively depend on the number of ICs chosen. The cross-correlation of the residuals and the foregrounds of the 1hr-field show very similar behaviour.

5 3D POWER SPECTRUM RESULTS

5.1 Auto-Correlations

In this section, we present the results of the 3d power spectrum estimation from the GBT intensity maps. There are three different error estimates on the intensity mapping power spectrum measurements as shown in Fig. 8:

- We use the auto correlations of the residual maps as a proxy for the noise power spectrum and insert it into Eq. 4 (solid error bar).
- We use the power spectrum of the difference of the maps divided by $\sqrt{2}$ as a proxy for the noise power spectrum and insert it into Eq. 4 (dashed error bar).
- We calculate the standard deviation of the sub-dataset cross-correlation power spectra and divide it by $\sqrt{6}$ to produce an error in the mean (dotted error bar).

The error based on the noise estimate of the difference maps (black dashed line) evidently is higher than the other two error estimates. We believe that this gives an upper limit on the error on the measurements since it includes systematic effects also correlated to the foregrounds which FASTICA partially subtracts from the data. The noise estimate of the

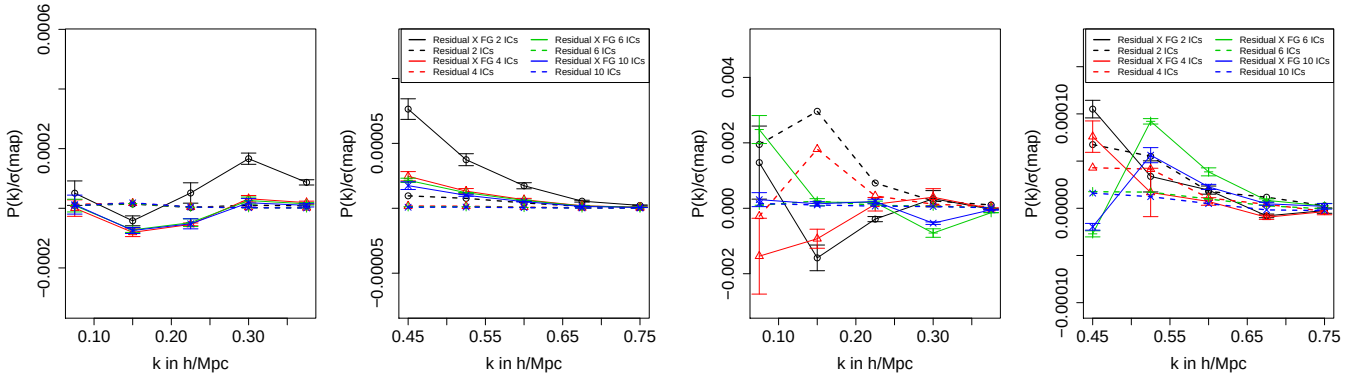

(a) Frequency bins 80-99; no mask

(b) Frequency bins 80-99; edges masked

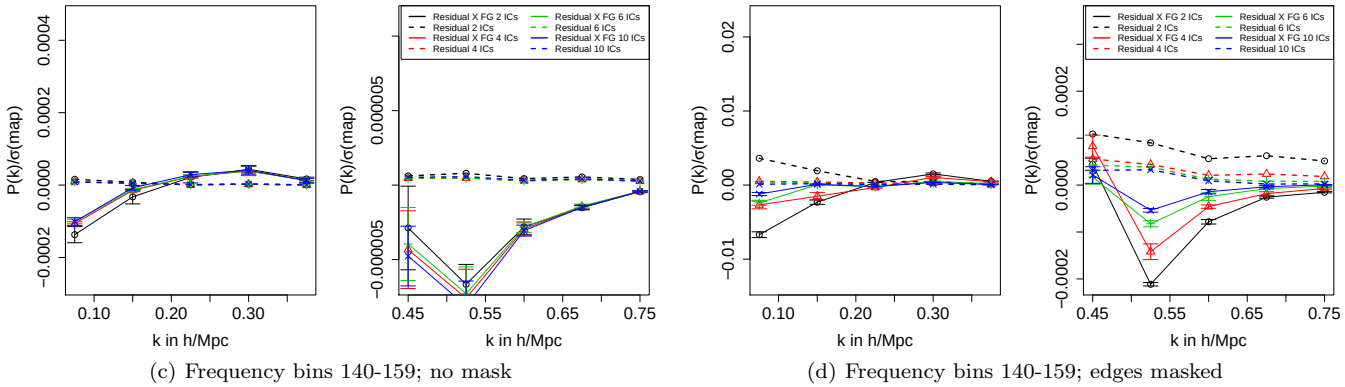

(c) Frequency bins 140-159; no mask

(d) Frequency bins 140-159; edges masked

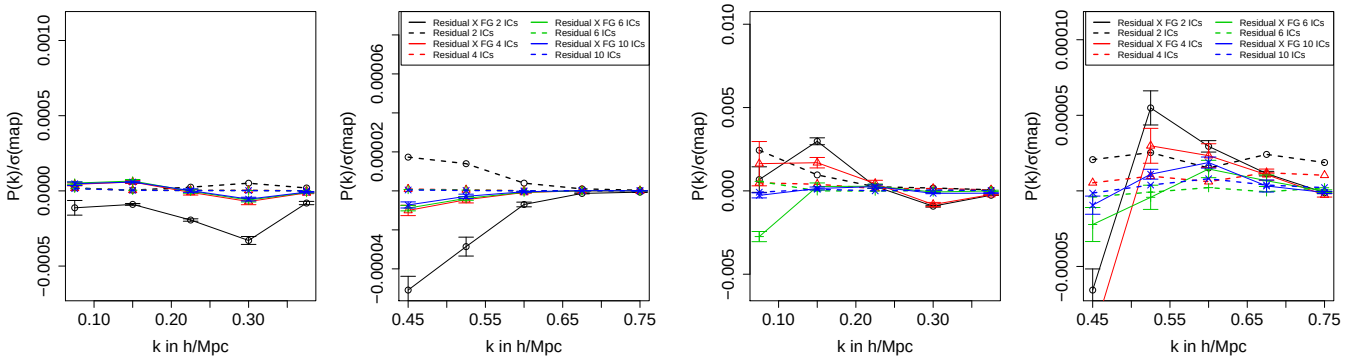

(e) Frequency bins 220-239; no mask

(f) Frequency bins 220-239; edges masked

Figure 7. The spatial 2d cross correlation between reconstructed foregrounds and residuals of the 15hr-field marked as the solid lines for different number of ICs with different colors. The dashed lines represent the residual power spectrum between sub-datasets. Each subfigure shows the 2d power spectrum with two different scales for large and small wavenumbers k. The correlations in each row are estimated over three frequency ranges each containing 20 bins. The first column of 2 panels is for a full map analysis and the second one for a masked analysis.

auto-correlation gives a better approximation of the errors on the foreground-subtracted measurements.

In Fig. 9, we present the intensity mapping power spectrum estimates for different number of ICs used for the foreground subtraction in comparison with the results published in SW13 marked by grey symbols. The estimates are the average of all possible combinations of the cross-power spectra between the 4 sub-datasets and the different error bar estimates as shown in Fig. 8 with the respective line styles. The power spectra converge for increasing number of ICs thus showing that that FASTICA is a robust method to remove the non-Gaussian foregrounds. In Fig. 9(a), the presented power spectrum of the 15hr-field is in reasonable agreement with the results in SW13 on large scales with $k < 0.2h\mathrm{Mpc}^{-1}$ but

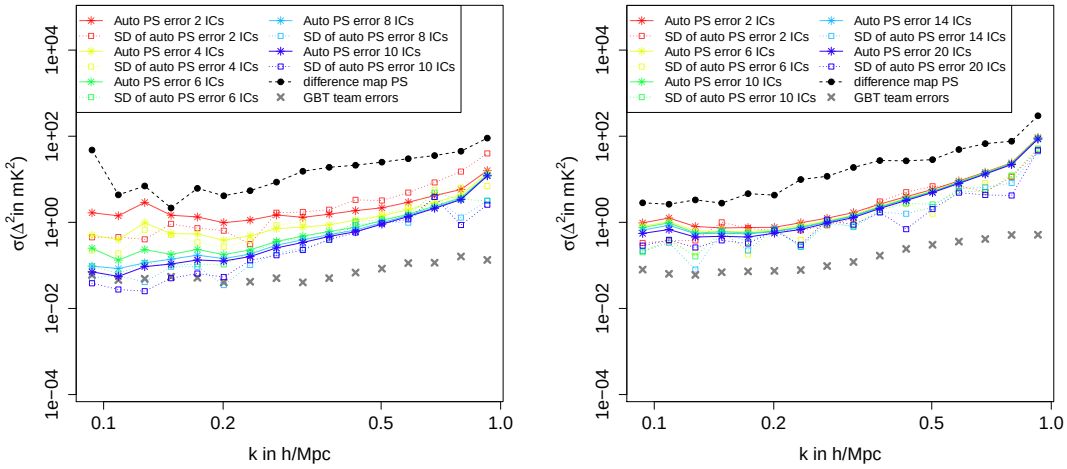
Auto PS error 2 ICs
SD of auto PS error 2 ICs
Auto PS error 4 ICs
SD of auto PS error 4 ICs
Auto PS error 6 ICs
SD of auto PS error 6 ICs
Auto PS error 8 ICs
SD of auto PS error 8 ICs
Auto PS error 10 ICs
SD of auto PS error 10 ICs
difference map PS
GBT team errors
σ(Δ²in mK²)
k in h/Mpc
Auto PS error 2 ICs
SD of auto PS error 2 ICs
Auto PS error 6 ICs
SD of auto PS error 6 ICs
Auto PS error 10 ICs
SD of auto PS error 10 ICs
Auto PS error 14 ICs
SD of auto PS error 14 ICs
Auto PS error 20 ICs
SD of auto PS error 20 ICs
difference map PS
GBT team errors
σ(Δ²in mK²)
k in h/Mpc

(a) 15hr-field (b) 1hr-field

Figure 8. The different error estimates of the 3d power spectrum measurement are shown in detail for different number of ICs for the 15hr-field and 1hr-field. The black dashed line is the error estimate based on the difference-maps. The solid coloured line the error based on the auto-correlations of the sub-dataset and the dotted coloured line are given by the standard deviation of the three cross-correlation measurements. The error estimates of the SW13 are marked with grey crosses.

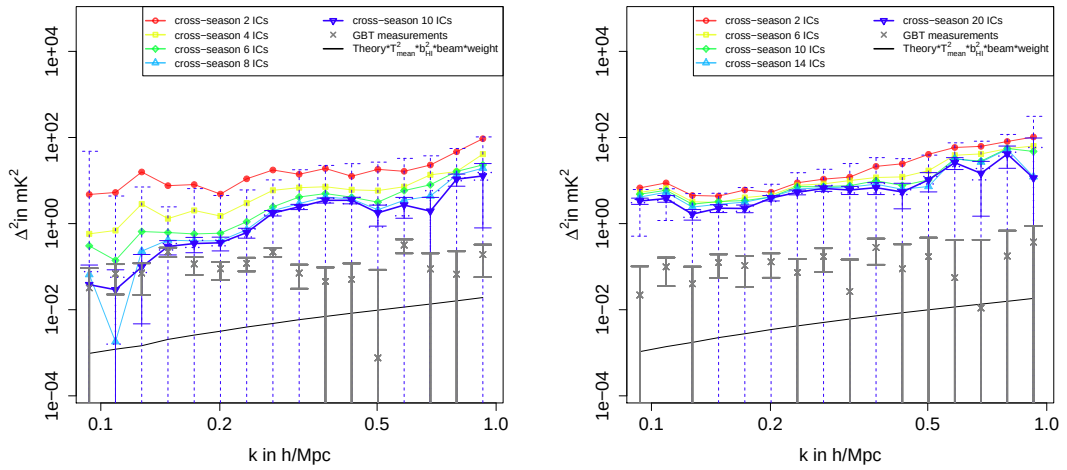

(a) 15hr-field (b) 1hr-field

Figure 9. 3d intensity mapping power spectrum cross-correlation between sub-datasets of the 15hr field data is shown in the left panel and for the 1hr field data in right panel with different error bar estimates as shown in Fig. 8 with the respective line styles. The measurements of the SW13 are marked with grey crosses. The black line is the theoretical model convolved with the window functions as described in 3.2 for a HI model with $\Omega_{\rm HI} b_{\rm HI} = 0.43 \cdot 10^{-3}$.

diverges for scales smaller than that. The amplitude of power spectrum of the 1hr-field is higher on all scales than previous measurements. We believe the differences are due to some residual foregrounds and the significant instrumental systematics in those maps. Any systematics which show Gaussian properties in the frequency domain are not removed by FASTICA which can lead to a non-Gaussian spatial structure in the foreground-subtracted maps. The individual Gaussian noise realisation of the different datasets should not correlate but the amplitude of the noise per pixel can be correlated to the amplitude of the overall signal which is dominated by the foregrounds. We believe this effect contributes to the high amplitude of the intensity mapping power spectrum measured by FASTICA.

This is in contrast to the SVD method which removes modes with high amplitudes regardless of their statistical properties. The GBT measurements are corrected for signal loss by an anisotropic transfer function $T(k_\perp, k_\parallel)$, for more details we refer the reader to Switzer et al. (2015). The power spectrum of the FASTICA-cleaned data does not require any corrections by a transfer function since the signal loss is negligible as shown in Wolz et al. (2014).

In general, the auto-correlations of the 15hr- and 1hr-fields are high compared to the theoretical prediction. This discrepancy could be explained in several ways. Systematics left-over from the foreground subtraction could boost the amplitude of the power spectrum. Additional power could also be added to the 21cm signal by fluctuations introduced

by polarization leakage which are not picked up by FASTICA or SVD. Finally, they could also be due to a not optimal choice of $\Omega_{\rm HI} b_{\rm HI}$ which controls the amplitude of the power spectrum.

5.2 Cross-Correlation with WiggleZ

The cross-correlation power spectrum of the intensity maps with the WiggleZ galaxy survey for both fields is shown in Fig. 10 for range of different numbers of ICs. The error bars in this figure are given by the standard deviation of the estimates between the sub-datasets and empty symbols mark negative correlations. It can be seen how the cross power spectrum converges with increasing number of ICs for both fields and, thus, verifies that FASTICA does not subtract 21cm signal from the data.

In Fig. 11 we show the cross-correlation for both fields with 10 ICs and 20 ICs, respectively, in comparison to the results of MA13 which are marked with blue and green shaded areas. Negative cross-correlations are indicated with empty symbols. Fig.11(a) demonstrates that the 15hr field estimates are mostly within the errors in agreement with previous findings in MA13 confirming the results in the auto power spectrum measurements. Our estimates of the 1hr fields are higher on most scales indicating that the intensity maps suffer from systematic contaminations that can not be resolved by the application of FASTICA. We believe this is due to the high noise properties of the maps which can be diminished by a method such as SVD but not by FASTICA.

6 CONCLUSIONS

In this study, we present a thorough analysis of 2 fields of the intensity maps observed by the GBT and previously analysed in Masui et al. (2013) and Switzer et al. (2013). Our pipeline includes a Fourier-based, weighted power spectrum estimator for auto-correlations and cross-correlations with galaxy surveys. We remove the diffuse Galactic foregrounds and point source contaminations with FASTICA which separates components based on a measure of their non-Gaussianity. The subtraction fidelity and systematic errors are investigated for analyses with different numbers of ICs, showing that the residual maps converge to the same result. We explore different masking of the maps to reduce the strong noise contamination at the edges of the data cube.

We confirm that FASTICA is well suited to subtract the Galactic and non-Galactic foregrounds from intensity mapping data since, by construction, it does not remove 21cm signal. We report that the power spectrum of the cleaned maps is independent of the number of ICs higher than 6 and therefore robust against parameter choices. The auto-correlation of the intensity maps typically has a higher amplitude in comparison with previous results by the GBT team which is within expectations since FASTICA is a very conservative removal technique compared to the indiscriminate SVD method. Both techniques measure auto-correlation power significantly above our current best guess at the cosmological signal which indicates severe systematic contaminations in the current datasets. The cross-correlation power with the WiggleZ galaxy survey converges with the increasing number of ICs and exhibits an about a magnitude higher amplitude than the GBT team measurements in some modes which could be caused by a correlation of the residual systematics with the galaxy distribution. We conclude that no transfer function is required when subtracting foregrounds with FASTICA since it exclusively removes those components which are non-Gaussian, however, this can lead to residual systematics caused by anisotropic noise boosting the power of the signal. In future work, we are planing to combine both techniques in order to exploit their individual advantages in the data reduction.

ACKNOWLEDGMENTS

Parts of this research were conducted by the Australian Research Council Centre of Excellence for All-sky Astrophysics (CAASTRO), through project number CE110001020. CB acknowledges the support of the Australian Research Council through the award of a Future Fellowship.

REFERENCES

Ansari R., Le Goff J. ., Magneville C., Moniez M., Palanque-Delabrouille N., Rich J., Ruhlmann-Kleider V., Yèche C., 2008, ArXiv e-prints 0807.3614

Battye R. A., Davies R. D., Weller J., 2004, MNRAS, 355, 1339

Blake C., Baldry I. K., Bland-Hawthorn J., Christodoulou L., Colless M., Conselice C., Driver S. P., Hopkins A. M., Liske J., Loveday J., Norberg P., Peacock J. A., Poole G. B., Robotham A. S. G., 2013, MNRAS, 436, 3089

Blake C., Brough S., Colless M., Couch W., Croom S., Davis T., Drinkwater M. J., Forster K., Glazebrook K., Jelliffe B., et al., 2010, MNRAS, 406, 803

Bull P., Ferreira P. G., Patel P., Santos M. G., 2014, ArXiv e-prints

Chang T.-C., Pen U.-L., Bandura K., Peterson J. B., 2010, Nature, 466, 463

Chang T.-C., Pen U.-L., Peterson J. B., McDonald P., 2008, Phys.Rev.Lett., 100, 091303

Chapman E., Abdalla F. B., Harker G., Jelic V., Labropoulos P., et al., 2012, MNRAS, 423, 2518

Drinkwater M. J., Jurek R. J., Blake C., Woods D., Pimbblet K. A., Glazebrook K., Sharp R., Pracy M. B., Brough S., Colless M., et al., 2010, MNRAS, 401, 1429

Eisenstein D. J., et al., 2005, ApJ, 633, 560

Gong Y., Chen X., Silva M., Cooray A., Santos M. G., 2011, ApJ, 740, L20

Hyvärinen A., 1999, IEEE Transactions on Neural Networks, 10, 626

Lewis A., Challinor A., Lasenby A., 2000, Astrophys. J., 538, 473

Lidz A., Furlanetto S. R., Oh S. P., Aguirre J., Chang T.-C., Doré O., Pritchard J. R., 2011, ApJ, 741, 70

Maino D., Farusi A., Baccigalupi C., Perrotta F., Banday A. J., Bedini L., Burigana C., De Zotti G., Górski K. M., Salerno E., 2002, MNRAS, 334, 53

Masui K. W., Switzer E. R., Banavar N. andBandura K., Blake C., Calin L.-M., Chang T.-C., Chen X., Li Y.-C., Liao Y.-W., Natarajan A., Pen U.-L., Peterson J. B., Shaw J. R., Voytek T. C., 2013, ApJ, 763, L20

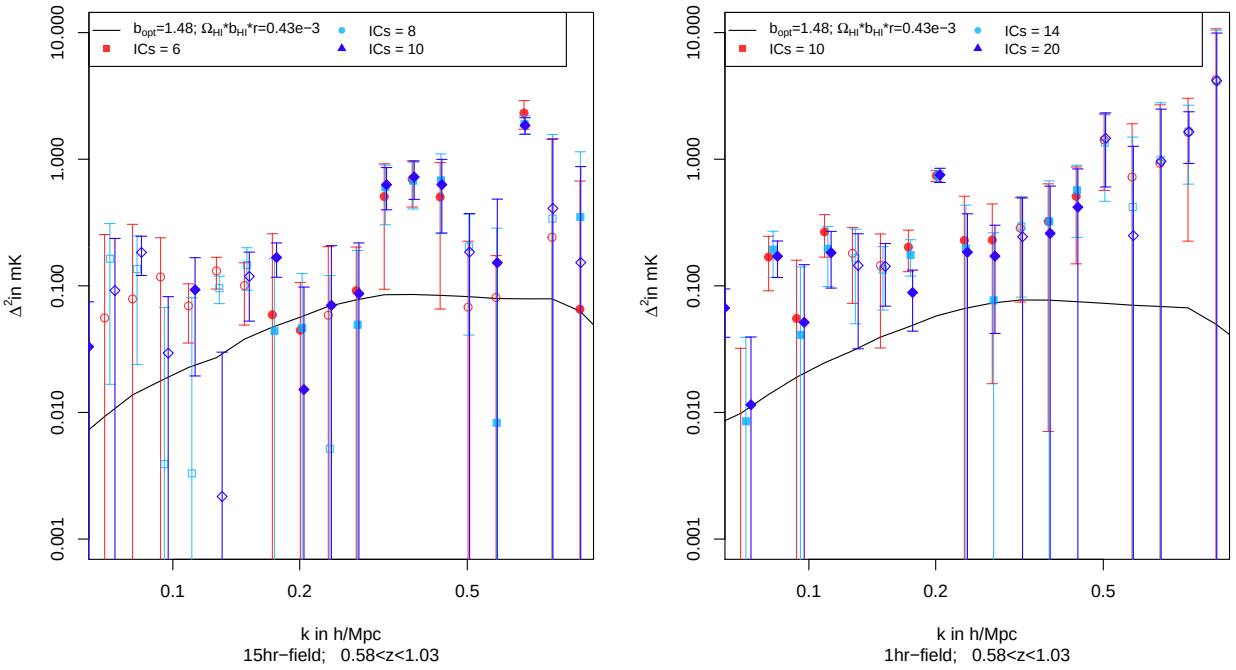

Figure 10. 3d cross-correlation between intensity maps and WiggleZ galaxies for foreground subtraction with different number of ICs for the 15hr-field in the left panels and the 1hr-field in the right panel.The black lines are the theoretical model convolved with the respective window functions of the weight function of the intensity maps and the selection function of the WiggleZ survey for a HI model with $\Omega_{\rm HI} b_{\rm HI} = 0.43 \cdot 10^{-3}$.

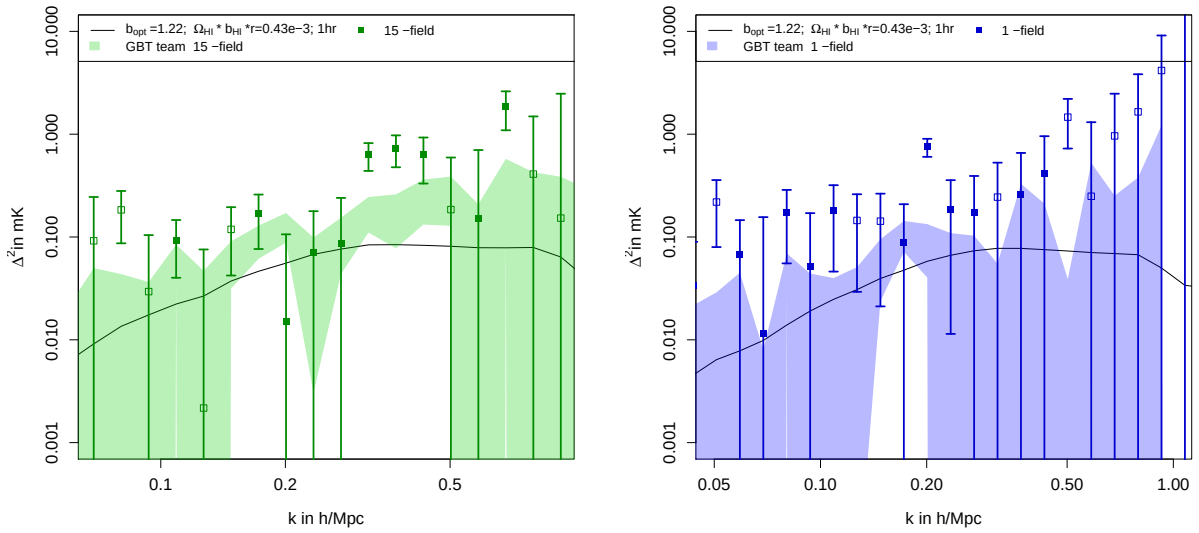

(a) 10 ICs; 15hr-field

(b) 20 ICs; 1hr-field

Figure 11. 3d cross-correlation between intensity maps and WiggleZ galaxies for foreground subtraction with 10 ICs in the left window for the 15hr-field and 20 ICs in the right window for the 1hr-field in comparison with the GBT results of MA13 marked by the shaded areas.The black lines are the theoretical model convolved with the respective window functions of the weight function of the intensity maps and the selection function of the WiggleZ survey for a HI model with $\Omega_{\rm HI} b_{\rm HI} = 0.43 \cdot 10^{-3}$.

Percival W. J., Cole S., Eisenstein D. J., Nichol R. C., Peacock J. A., et al., 2007, MNRAS, 381, 1053
Percival W. J., Reid B. A., Eisenstein D. J., Bahcall N. A., Budavari T., Frieman J. A., Fukugita M., Gunn J. E., Ivezić Ž., Knapp G. R., Kron R. G., Loveday J., Lupton R. H., 2010, MNRAS, 401, 2148
Peterson J. B., Suarez E., 2012, ArXiv e-prints 1206.0143
Planck Collaboration X, 2015
Planck Collaboration XXV, 2015
Pullen A., Dore O., Bock J., 2013, ArXiv e-prints 1309.2295
Shaw J. R., Sigurdson K., Pen U.-L., Stebbins A., Sitwell M., 2014, ApJ, 781, 57
Shaw J. R., Sigurdson K., Sitwell M., Stebbins A., Pen U.-L., 2014, ArXiv e-prints
Switzer E. R., Chang T.-C., Masui K. W., Pen U.-L., Voytek T. C., 2015
Switzer E. R., Masui K. W., Bandura K., Calin L.-M., Chang T.-C., Chen X.-L., Li Y.-C., Liao Y.-W., Natarajan A., Pen U.-L., Peterson J. B., Shaw J. R., Voytek T. C., 2013, MNRAS, 434, L46
Tegmark M., 1997, ApJ, 480, L87
Tegmark M., et al., 2004, Astrophys. J., 606, 702
Vujanovic G., Staveley-Smith L., Pen U.-L., Chang T.-C., Peterson J., 2009, ATNF Proposal, p. 2491
White M., Song Y.-S., Percival W. J., 2009, MNRAS, 397, 1348
Wolz L., Abdalla F. B., Blake C., Shaw J. R., Chapman E., Rawlings S., 2014, Mon. Not. Roy. Astron. Soc., 441, 3271
Wyithe S., Loeb A., Geil P., 2007, MNRAS